nature communications

Article

https://doi.org/10.1038/s41467-025-67064-1

Optically-controlled phonon-specific phase transitions from graphite to diamond

Received: 14 July 2025

Accepted: 21 November 2025

Published online: 09 December 2025

Check for updates

Yunzhe Jia[1,2], Chenchen Song[1,2], Daqiang Chen[1,2], Qing Chen[1,2], Cui Zhang[1,3] & Sheng Meng[1,2,3]

Controlling phase transition processes and the atomic structure of new states with light has emerged as a highly challenging frontiers in condensed matter physics and materials science. The conversion of graphite to diamond typically relies on high-pressure and high-temperature conditions, while the advent of ultrafast laser has opened entirely new possibilities for dynamically controlling such structural transformation under non-thermodynamic state. Herein, employing state-of-the-art first-principles non-adiabatic molecular dynamics simulations, we elucidate ultrafast pathways of light-induced graphite-to-diamond phase transition and reveal the laws governing the selective formation of cubic or hexagonal diamond, as well as their subsequent structural evolution, by regulating laser parameters. Such optically controlled diamond formation stems from early-stage structural reconstruction driven by electron-phonon couplings and indirect excitation of specific phonon modes (e.g. B_{3g}^2 modes) via phonon-phonon couplings. The competition between newly generated phonons from indirect excitation constitutes the key factor determining the fine structure of final product. This work not only demonstrates effective modulation of structural phase transition through photoinduced non-thermal pathways, but also provides important strategy for efficient and eco-friendly material synthesis via optical control.

The conversion dynamics of graphite-to-diamond and their underlying mechanisms have been the subject of extensive research[1–7]. Such phase transitions between carbon allotropes involve alterations in the bonding pattern of carbon atoms. To achieve precise control over material structures and thereby synthesize new carbon materials with unique properties, it is crucial to understand the intrinsic driving forces behind structural evolution and the means of reaction regulation.

High pressure can effectively reduce the free energy barrier of phase transitions[8], therefore, earlier studies have mainly focused on converting graphite into diamond under high pressure[9–13], followed by research utilizing of shock waves[14–19]. Over half a century ago, Bundy et al. reported the successful synthesis of man-made cubic diamond (CD)[9] and hexagonal diamond (HD)[13] under high-pressure, high-temperature (HPHT) conditions, with synthesis temperatures exceeding 2000 °C and 1000 °C, respectively. Recently, the breakthrough in successfully synthesizing nano-sized, high-purity HD from graphite under HPHT conditions has further advanced the research progress in engineering the desirable features of carbon allotropes[3,20]. In 1961, shock-induced graphite-to-diamond phase transitions were also reported in ref. 14. The microscopic mechanisms underlying graphite-to-diamond phase transition under pressure[1,3,21–23] and shock waves[2,24,25] remain a focus of research to this day. For instance, Armstrong et al. observed the phase transition process in shock compressed graphite on picosecond timescale using X-ray diffraction, and found that the formation of HD is kinetically more favorable than that of CD under rapid compression[19]; while Chen et al., from the

[1]Beijing National Laboratory for Condensed Matter Physics and Institute of Physics, Chinese Academy of Sciences, Beijing, China. [2]School of Physical Sciences, University of Chinese Academy of Sciences, Beijing, China. [3]Songshan Lake Materials Laboratory, Dongguan, Guangdong, China.
e-mail: cuizhang@iphy.ac.cn; smeng@iphy.ac.cn

perspective of computational research, further clarified that different interlayer sliding distances may lead to different products during shock-induced phase transitions[2].

Following the successive experimental and theoretical reports on the induction of graphite-to-diamond transition via hole doping of the valence bands at room temperature[26,27], experimental and theoretical explorations into photoinduced graphite-to-diamond phase transition have been initiated. Raman et al. clearly captured the process of photoinduced interlayer compression leading to bond formation using electron diffraction techniques[28]. Carbone et al. detected signals of interlayer bond formation around ~180 fs after photoexcitation via fs-resolved electron energy loss spectroscopy[29]. Nüske et al. observed the formation of nanoscale cubic diamond crystals in the laser-irradiated highly oriented pyrolytic graphite (HOPG) sample using Raman spectroscopy and *X*-ray diffraction[7]. Duan et al. observed ultrafast formation of a transient two-dimensional diamond-like structure under femtosecond laser irradiation using MeV ultrafast electron diffraction[30]. Furthermore, several STM-based studies have identified the regions of laser-excited sp^3-bonded domain formation involving interlayer sliding, intralayer buckling, and periodic interlayer bonding[31,32]. Meanwhile, computational studies on the formation mechanism of photoinduced interlayer bonding in graphite have been emerging[30,33–35]. Luo et al. emphasized the significance of the stacking mode in influencing the bonding patterns between adjacent graphite layers and the formation of different final structures[30]. Song et al. demonstrated a non-adiabatic dynamic process of forming sp^3-hybridized carbon structures within a few hundred femtoseconds after laser irradiation and highlighted the importance of electron–phonon coupling in such processes[34]. However, there remains a substantial gap in unraveling the reaction pathways and the key mechanisms of light-induced graphite-to-diamond phase transition under nonequilibrium regimes on ultrafast timescales, and the microscopic dynamic picture of such phenomena continues to be a fascinating challenge.

Given the current lack of a comprehensive reaction pathway of light-induced graphite-to-diamond conversion and an understanding of the intrinsic mechanisms of such reactions on ultrafast timescales, we herein report the nonequilibrium reaction dynamics of photogenerated charge carriers and lattice motions in such transitions, as well as how the excitation modes are correlated to the ultimately formed diamond atomic structures. Through state-of-the-art first-principles non-adiabatic excited-state dynamics simulations, we reveal the complete reaction pathway diagram of light-driven graphite-to-diamond phase transitions, as illustrated in Fig. 1. The phase transition pathway and final structure are closely correlated with the proportion of photoexcited electrons. Excessive excitation leads to the formation of an amorphous state, while insufficient excitation fails to drive the graphite structure to overcome the reaction energy barrier and complete the phase transition. An appropriate amount of electron excitation is crucial for the formation of the diamond structure. Our results demonstrate the rational control of the phase transition process and products by optical means. Under the action of the laser field, electron–phonon coupling induces specific phonon displacements, thereby giving rise to different degrees of interlayer sliding and bonding modes. In particular, the strong excitation of B_{3g}^2 and TO-5 phonon modes guides the selective formation of cubic and hexagonal diamonds, respectively. We find that the final fine carbon structure of the phase transition is strongly correlated with the degree of excitation and propose a light wavelength-fluence phase diagram for photoinduced diamond generation, which reveals the optical regulation capability of ultrafast lasers with appropriate light field conditions on the phase transition process. Our results highlight the subtle nonequilibrium reaction pathways and intrinsic dynamic mechanism of laser-induced graphite-to-diamond phase transition, providing new insights and directions for achieving precise optical control of the atomic structure of materials.

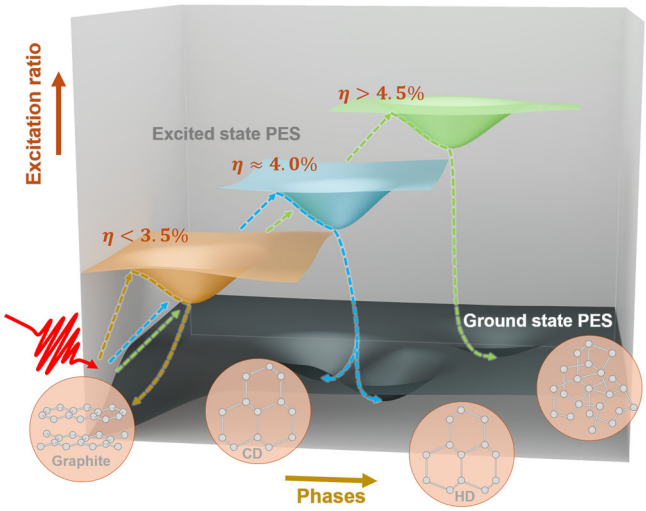

Fig. 1 | Schematic diagram of light-driven graphite-to-diamond phase transition. Optical control over the transition pathways between the initial graphite structure and the final reaction products can be achieved on ultrafast timescales (hundreds of femtoseconds) by manipulating the electronic excitation amount η. The three excited-state potential energy surfaces with different electron excitation ratios are depicted in orange, blue, and green, respectively, corresponding to different phase transition pathways and products.

Results

Nonequilibrium pathways of light-induced graphite-to-diamond phase transition

We first apply a Gaussian-shaped laser pulse with a photon energy of 1.55 eV and a maximum field strength of E_0 = 0.514 V/Å on the *AB* stacked graphite crystal. The laser pulse is polarized along the armchair direction of graphite with a fluence of 120.5 mJ/cm^2, which is below the previously reported optical damage thresholds of 130–250 mJ/cm^2 for graphite[28,36–38]. The nonequilibrium reaction pathway of light-induced transition from graphite to diamond is reported in Fig. 2, whereas the characteristic atomic structures and the corresponding energy changes during the reaction are displayed in Fig. 2a. Atomic structures in the insets are extracted directly from the trajectory of non-adiabatic molecular dynamic simulations, representing the structure characteristic of different stages of the phase transition: (i) initial graphite structure, (ii) interlayer contraction after excitation, (iii) intralayer buckling, (iv) formation of sp^3 bonds, (v) generation of diamond-like structure, and (vi) the final structure of phase transition, respectively. The calculated single-point energy of corresponding structures indicates that a potential energy barrier of ~1.0 eV/atom needs to be overcome for such photoinduced phase transition reaction. Upon photoexcitation, the electronic structure significantly changes from ~100 fs (see Suppl. Fig. 1) and opens an energy band gap of ~3.27 eV at 250 fs, which represents the electronic signature of the formed sp^3-hybridized carbon network.

To further trace the structural relaxation process and identify the stable final products of the phase transition, we apply a thermal bath to anneal the photoexcited system down to room temperature at an annealing rate of 300 K/ps, as shown in the Suppl. Fig. 2. The annealing process starts from the state obtained at 400 fs in the non-adiabatic simulation and continues up to 8.0 ps after the temperature reaches ~300 K. Such annealing process addresses, to some extent, the issue of insufficient energy dissipation in non-adiabatic excited-state simulations and provides an approach to access the ultimate stable structure after photoexcitation relaxation, since the evolution of lattice structures typically takes at least a few picoseconds to complete[39,40]. Meanwhile, the annealing relaxation process also mimics the diffusion and dissipation of energy from the local lattice structure to the

https://doi.org/10.1038/s41467-025-67064-1

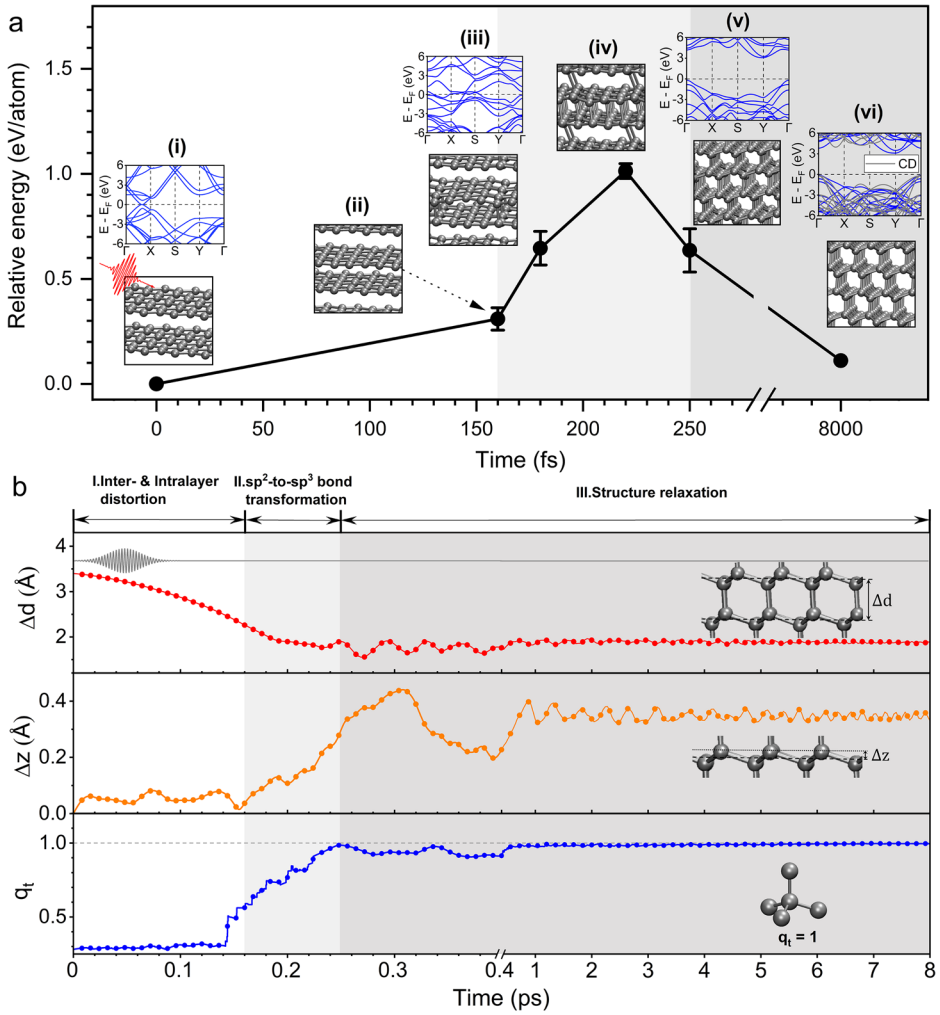

Fig. 2 | Light-driven graphite-to-diamond phase transition pathway. a Energy profiles of the graphite-to-diamond phase transition. The error bars are derived from five independent TDDFT trajectories under the same conditions. The insets (i–vi) illustrate the evolution of the atomic structure as well as the changes in the electronic structure during the phase transition. The band structure of cubic diamond is shown by gray lines in inset (vi). **b** Time evolution of the interlayer spacing Δd, intralayer buckling height Δz and tetrahedral order parameter q_t of graphite. The insets are schematic diagrams of the three parameters. The Gaussian-shaped laser field waveform is also shown, with a photon energy of 1.55 eV, a full width at half maximum (FWHM) of 30 fs, and a maximum strength of $E_0 = 0.514$V/A at 48 fs.

surrounding regions in practical scenarios. As shown in Fig. 2a, through the annealing relaxation, the metastable sp^3-hybridized carbon lattice further evolves into a stable CD crystal structure, exhibiting a band gap that is further widened to 3.63 eV, and its electronic band structure can be directly compared with that of perfect CD.

To obtain the microscopic dynamics information of sp^2-*to*-sp^3 phase transition, the time variation of three structural parameters, namely, graphite interlayer distance Δd, the intralayer buckling height Δz and tetrahedral order parameter q_t, are presented in Fig. 2b. The tetrahedral order parameter q_t is defined as[41]

$$q_t = \langle q_t(k) \rangle_k = \left\langle 1 - \frac{3}{8} \sum_{i=1}^{3} \sum_{j=i+1}^{4} \left(\cos\theta_{ikj} + \frac{1}{3} \right)^2 \right\rangle_k \quad (1)$$

where θ_{ikj} is the angle formed by the kth atom and its nearest neighbors i and j. The q_t accurately characterizes the structural similarity of the intermediate state generated during photoexcited sp^2-*to*-sp^3 phase transition with that of perfect diamond. For a perfect tetrahedral configuration at 0 K, $\cos\theta_{ikj}$ is equal to $-\frac{1}{3}$, yielding $q_t = 1$ for diamond, as illustrated in Fig. 2b.

Upon light irradiation, the graphite layer spacing Δd undergoes a rapid compression from 3.4 Å to ~2.3 Å within 160 fs. A pronounced sp^2-*to*-sp^3 structure transformation initiates at around 160 fs. Such ultrafast interlayer compression and sliding processes in graphite under light irradiation have been widely observed in previous experiments[7,28,30–32], and the timescale for the initial formation of sp^3 bonds is also consistent with the ~180 fs reported in previous experiments[29]. From then on, the interlayer distance Δd further reduces to ~1.9 Å, while the buckling height Δz, which characterizes the degree of out-of-plane distortion, rapidly increases to more than 0.3 Å. Such structural changes in graphite provide the necessary spatial conditions for the formation of interlayer sp^3 bonds. According to the criterion that a chemical bond forms once the distance between two carbon atoms in adjacent layers is less than 1.8 Å, interlayer C-C bonds start to form rapidly from 160 fs onwards, with the average number of interlayer bonds N_{IB} reaching ~4 at ~250 fs (Suppl. Fig. 3). The analysis of time-dependent electron localization function and differential charge density, as shown in Suppl. Figs. 4, 5, provide further electronic evidence for the formation of sp^3 bonds. The time evolution of the tetrahedral order parameter q_t, shown in Fig. 2b, suggests that graphite evolves into a diamond-like structure very close to the

https://doi.org/10.1038/s41467-025-67064-1

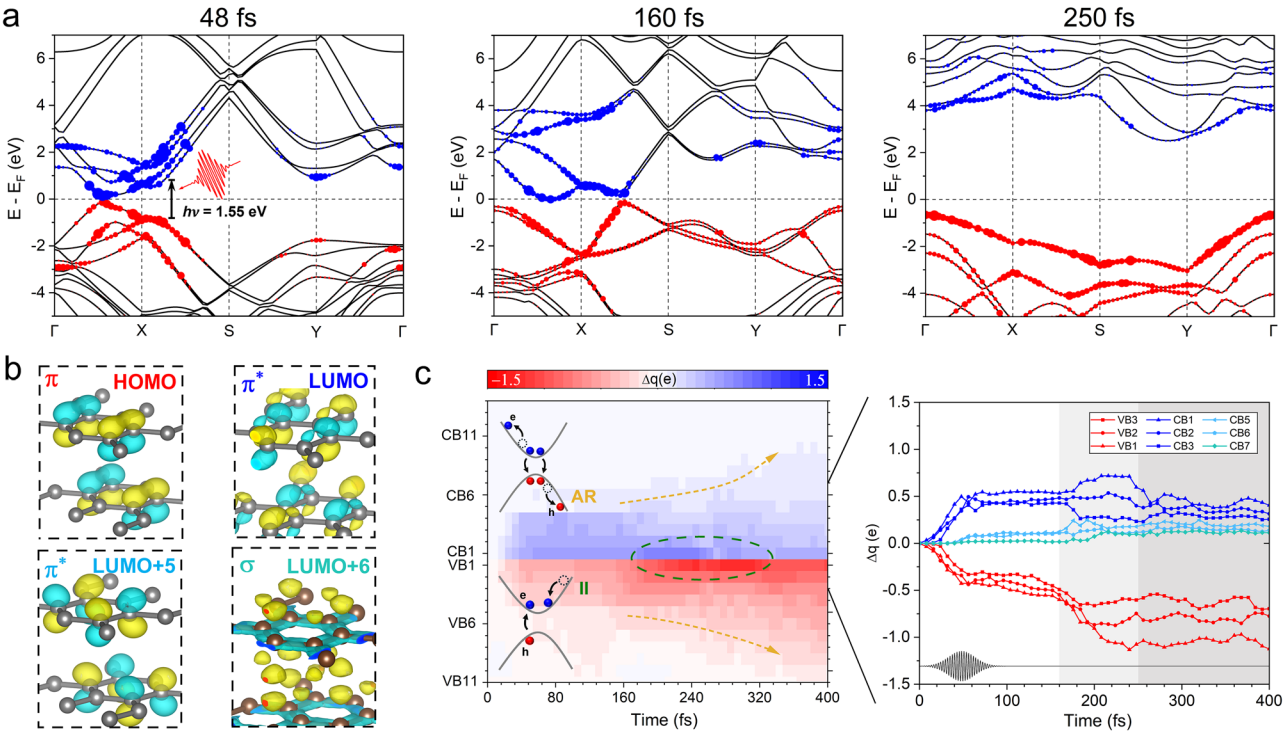

Fig. 3 | Electronic origin of the sp^2-*to*-sp^3 phase transition. a Excited band structure of light-induced graphite-to-diamond phase transition. The configurations are extracted from the non-adiabatic molecular dynamics simulations at 48, 160, and 250 fs, respectively, corresponding to three distinct phase transition stages. The sizes of blue and red dots are in proportion to the square of the population of excited electrons and holes generated by the laser pulse with respect to the ground state. (The largest dot represents $\Delta q \approx 1.92\ e$). **b** Diagrams of selected molecular orbitals, corresponding to π, π^* and σ types. **c** Distribution of the photogenerated charge carrier occupancy (Δq) in each molecular orbital as a function of time. Valence bands are counted by energy relative to the Fermi level in decreasing order, while conduction bands are counted by energy relative to the Fermi level in increasing order. The insets are schematic diagrams illustrating the mechanisms of Auger recombination (AR, orange dashed arrow) and impact ionization (II, green dashed circle) processes in the phase transition. The time evolution of carrier occupancy in molecular orbitals near the Fermi level, from valence band 3 (VB3) to conduction band 7 (CB7) is highlighted on the right.

tetrahedral configuration within ~250 fs after photoexcitation. Until 400 fs, Δd remains below 2.0 Å, N_{IB} stabilizes at 4 with minimal fluctuations, and q_t varies around 0.95, all of which imply that the light-induced diamond-like structure enters a structural metastable state.

During the subsequent annealing process, the interlayer spacing Δd, buckling height Δz and the number of interlayer bonds N_{IB} stabilize at ~2.0, ~0.35 Å and 4, respectively. In contrast, the tetrahedral order parameter q_t rises from ~0.95 to 1, which clearly indicates that the metastable diamond-like structure relaxes into a perfect CD structure and acquires an electronic band structure very similar to that of CD. To verify the influence of initial state selection on the annealing processes, we extract another configuration from the rt-TDDFT trajectory at 280 fs as the initial state for the thermal relaxation process, as shown in the Suppl. Fig. 6. A comparison of Fig. 2b and Suppl. Fig. 6 reveals that although the relaxation processes initiated from different excited-state configurations exhibit subtle differences in specific dynamic behaviors, the final phase transition structure remains unaffected.

Given the features of the atomic and electronic structure evolution, we propose the laser-induced phase transition from graphite to diamond undergoes three distinct key stages: (i) structure distortion of graphite; (ii) sp^2-*to*-sp^3 bonding transition; (iii) relaxation into the ultimate phase, delineated by the different background colors in Fig. 2. It is worth mentioning that under the same laser excitation condition, *AA* stacked graphite undergoes a similar phase transition to *AB* stacked graphite (Suppl. Fig. 7).

Ultrafast dynamics of excited charge carriers

Based on the non-thermal reaction pathways of graphite-to-diamond conversion identified above, we next focus on elaborating the nonequilibrium dynamics of photogenerated charge carriers within the femtosecond timescale, which is crucial for initiating the phase transition. In Fig. 3a, we track the changes of electronic structures and photogenerated carrier distribution along the light-induced carbon structure conversion and present the corresponding electronic states at each of the three stages. The blue and red dots represent the photogenerated electrons and holes, respectively, and the size of the dots depicts the population of excited charge carriers. Under the ultrafast laser pulse with a photon energy of 1.55 eV and a fluence of 120 mJ/cm^2, the electron subsystem of graphite is boosted immediately in the vicinity of a high symmetry point, with both resonance excitation and multiphoton absorption observed. The percentage of excited electrons reaches a maximum of about 3.8% during the direct action of laser light (see Suppl. Fig. 8). By the end of the first stage of phase transition at 160 fs, the electrons excited from the π band to the π^* band have scattered into the unoccupied σ interlayer band, as shown in Fig. 3b. Such redistribution of photogenerated electrons accounts for the weakening of in-plane C-C bonds, resulting in the lattice instability of graphite and promoting the out-of-plane distortion.

We further carry out a thorough analysis of the carrier occupancy in each electronic state during the light-induced process. Temporal evolution of the distribution of the photogenerated charge carriers (Δq) in each orbital is presented in Fig. 3c. We find that starting from ~100 fs after the end of light irradiation, a small fraction of photoexcited electrons is scattered to high-energy orbitals, as indicated by the orange arrow in Fig. 3c. The new distribution is the result of Auger recombination (AR), in which the excess energy released by electron-hole recombination scatters electrons to higher energy levels. On the other

https://doi.org/10.1038/s41467-025-67064-1

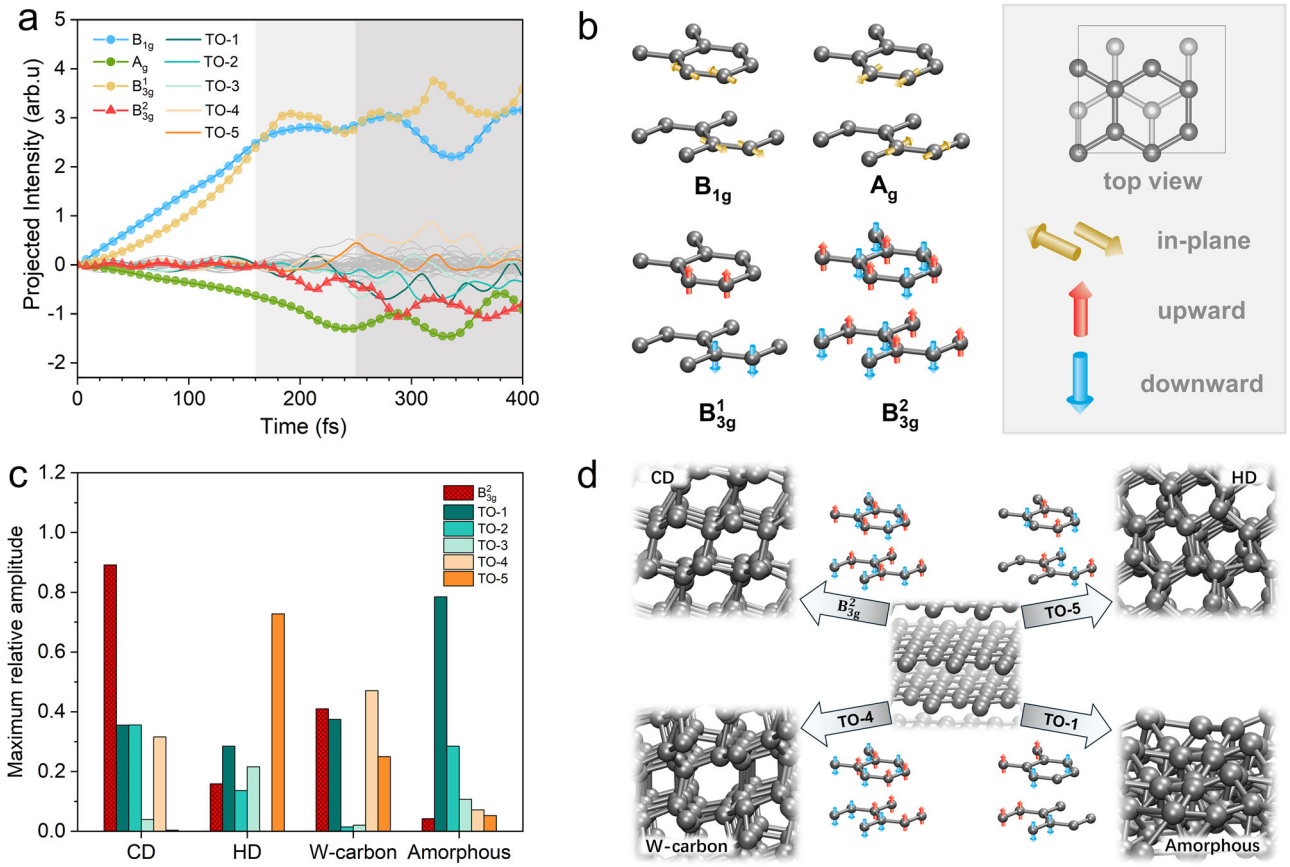

Fig. 4 | Dynamic phonon coupling and competition. a Time evolution of excited phonon modes at Γ point for the graphite phase transition to cubic diamond. The excitation degree of each phonon branch at each moment is characterized by projecting the atom displacement in the trajectory onto the corresponding phonon eigenvectors. **b** Vibrational modes of specific excited phonons. The colored arrows indicate the direction of atomic displacement of phonon modes. **c** Average amplitude of different excited phonons in the phase transition processes of various products. The amplitudes are obtained by averaging over the time period of 300 to 400 fs in different trajectories. **d** Schematic diagram of the relationship between the type of excited phonon mode and the final structure of the phase transition.

hand, in the second stage of phase transition (>160 fs), an increase of charge carriers is also observed near the Fermi level, highlighted by the green dashed line in Fig. 3c. It may be attributed to the energy release from high-energy electron collisions to create new electron-hole pairs, namely impact ionization (II), leading to an increase in charge carrier occupancy near the band edges. It is worth noting that although the Hamiltonian used in our non-adiabatic calculations does not explicitly include electron-electron scattering terms[42], the incorporation of multiple k-points and the presence of lattice distortions (or virtual phonons) allow electron scattering to be included to a certain extent. This enables us to capture the key Auger process and carrier transport. Since adiabatic TDDFT tends to underestimate the carrier-carrier interaction and the scattering rates in real systems to some extent, the actual electron-electron scattering effects might be more pronounced than what the current simulation results show.

Specifically, during the first stage of phase transition (<160 fs), photoexcitation occurs mainly between the three highest occupied orbitals and the three lowest unoccupied orbitals, that is, from valance band VB1-3 (counted in the order of decreasing energy from the Fermi level) to conduction band CB1-3 (counted in the order of increasing energy from the Fermi level), as shown by the blue and red curves in Fig. 3c. A small amount of excited charge occupation is also observed in CB5 and CB6 during this stage. In the second stage of phase transition where interlayer sp^3 bonds form, the charge carrier occupancy of VB2, VB1, CB1, CB2 increase significantly, while more electrons are scattered into high-energy orbitals, such as CB6 and CB7. Upon entering the relaxation stage at ~250 fs, ~2% of the photogenerated charge carriers are retained. The redistribution of photogenerated charge carriers is the result of the combined action of AR and II processes. Among them, AR is the dominant process that further scatters excited electrons into higher energy levels, thereby reducing the in-plane stability of graphite and promoting the formation of interlayer bonds.

Key role of specific phonon excitations

Based on the understanding of the electronic origin of the phase transition, we further investigate the lattice dynamics induced by the redistribution of photogenerated charge carriers through electron–phonon coupling, as well as the influence of excited phonon modes on the optical pathway of graphite-to-diamond conversion. Under light irradiation, the electronic subsystem of graphite is rapidly excited within tens of femtosecond, as shown in Fig. 3. To identify and track the emergence and evolution of excited phonons, we project the real-time displacement of carbon atoms onto the 48 phonon eigenvectors of the initial graphite structure. The projected intensity, shown in Fig. 4a, can be expressed as $\sum_i d_i \cdot u_{ij}$, where d_i is the displacement vector of the ith atom from the ground state at $t = 0$, and u_{ij} is the phonon eigenvector of the jth phonon branch.

We find that three phonon modes, i.e., B_{1g}, A_g and B_{3g}^1 modes, are gradually excited during the first stage of the phase transition, as demonstrated in Fig. 4b. The excited interlayer shearing modes B_{1g} and A_g are responsible for the occurrence of interlayer sliding in graphite,

which is the result of π-π* optical transition[43]. Another excited mode, B_{3g}^1, accounts for the interlayer compression of graphite. The excitation and cooperation of these specific phonon modes provide the necessary conditions for the initiation of the graphite-to-diamond phase transition. More intriguingly, starting from ~160 fs, a fourth phonon mode, namely B_{3g}^2, is gradually excited through phonon–phonon coupling, as indicated by the red triangles in Fig. 4a. This mode represents the out-of-plane non-resonant motions of carbon atoms that lead to the intralayer buckling of graphite. To further explicitly demonstrate the phonon–phonon coupling effects during the phase transition, we calculate the potential energy surfaces (PES) of B_{3g}^2 mode under the condition where the B_{3g}^1 mode exhibits different displacements. The results shown in the Suppl. Fig. 9 indicate that the intense excitation of B_{3g}^1 mode can effectively induce substantial changes in the PES of the B_{3g}^2 mode. The average atomic displacement $\langle \Delta r \rangle$ of the above four primarily excited phonon modes at Γ point is also calculated and presented in Suppl. Fig. 10, to further demonstrate the lattice dynamics and anharmonicity during the excitation and phase transition process in real space. Similar behaviors to those observed in the phonon projection plot have been observed, see Suppl. Fig. 10.

Since the interlayer spacing of the excited graphite system remains within 2 Å after 160 fs, adjacent layers begin to form interlayer sp^3 bonds through deformation, and metastable diamond-like (CD) structure appears at ~250 fs. In the light-induced formation of the CD structure, other transverse optical (TO) phonons are also induced to experience weak excitation from the second stage onwards. Similar coupling behaviors of multiple excited phonons have also been observed in other systems[44–47], for example, the coupling between in-plane and out-of-plane polarizations in ferroelectric material α-In_2Se_3[47].

The formation of different carbon allotropes (sp^3-bonded) from graphite is an issue of great interest. Our independent non-adiabatic excited-state dynamic trajectories obtained under different photoexcitation conditions suggest that CD, HD, and orthorhombic W-carbon with 5- and 7-membered rings could all be the outcomes of optically driven phase transitions in graphite. By comparing the types and intensities of excited phonons that result in different final carbon structures, we conclude that the excitation of the B_{1g}, A_g and B_{3g}^1 modes is a prerequisite for initiating the deformation of graphite structure and providing the essential lattice distortion for the formation of sp^3 bonds. Although we only observed the formation of the W-carbon under the laser conditions employed, different carbon allotropes[48–50] may also form when specific phonon modes are excited through the combined effects of electron–phonon coupling and phonon–phonon interactions.

There is a strong correlation between the structure of light-induced phase transition products and the four most strongly excited phonon modes. Figure 4c displays the average amplitudes of different excited phonons during the period of 300 to 400 fs, corresponding to the dynamic trajectories that lead to the formation of different final structures. By analyzing the excitation strengths of all six phonon modes selectively excited from the second stage of the phase transition, including B_{3g}^2 and five TO modes (also see Suppl. Fig. 11), we find that, compared to the other modes, the strongest excitations of B_{3g}^2, TO-5 and TO-4 modes dominate the generation of the CD, HD and W-carbon structure, respectively. As illustrated in Fig. 4d, the dependence of the light-driven product on the excitation phonons is the result of the competition between the excited phonon modes in the second stage of the phase transition after photoexcitation. The intrinsic vibrational modes of the most prominent phonons, coupled with the sliding and compression phonons excited in the first stage, determine the upper and lower alignments of the in-plane buckling and thus the final atomic structure of the phase transition product.

Optical regulation of phase transition

After addressing the driving forces and microscopic mechanism of light-induced graphite-to-diamond phase transition, we next explore how particular laser conditions affect the conversion of graphite to diamond. To distinguish the atomic structure of CD and HD, we further define a bond parameter Q, expressed as

$$Q = \langle Q_{mn} \rangle = \left\langle 1 - \frac{4}{3} \sum_{i=1}^{3} \left(\cos\left[\min\left(\left| \gamma_{imnj} \right| \right) \right] - \frac{1}{2} \right)^2 \right\rangle_{mn}, \quad j = 1, 2, 3 \tag{2}$$

where m and n represent the two carbon atoms of a specific C-C bond, and i and j are the other three nearest neighboring carbon atoms of m and n, respectively. For each atom i, the dihedral angle γ_{imnj} determined by the four atoms (i, m, n and j), has three possible values corresponding to three different j. The minimum values of $|\gamma_{imnj}|$ are 0° and 60° for standard overlapping or crossed carbon-carbon bonds, respectively. This means that the Q_{mn} value of a standard eclipsed C-C bond is 0, while that of a crossed C-C bond is 1, as illustrated in Suppl. Fig. 12. Therefore, the average Q value of all C-C bonds in CD and HD is close to 1 and 0.75, respectively. To clarify, the bond parameter Q is used to distinguish CD and HD structures, while the tetrahedral order parameter q_t characterizes the tetrahedral configuration in carbon structures.

In Fig. 5, we report that, at a pump wavelength of 800 nm (1.55 eV), the structures obtained from the light-driven phase transition exhibit a significant dependence on the laser fluence. The dashed lines indicate the approximate boundaries between the different carbon structures. The diagram suggests that CD is the main product of light-induced phase transition at laser fluences of ~120–130 mJ/cm², while graphite transforms into hexagonal diamond (HD) and W-type carbon when the fluence is above and below this range. In the case of fluence value below ~90 mJ/cm², the system lacks sufficient excitation energy to initiate the first stage of the phase transition. In contrast, when the laser power is excessively high, it results in the inability to properly excite the required phonon modes during the second stage of the reaction, and thus the crystalline structure fails to form.

We propose the wavelength-fluence phase diagram of the graphite-to-diamond transition in Fig. 5b, where the laser wavelength ranging from 600 to 1000 nm and the light fluence reaching the order of magnitude of 10^2 mJ/cm² are all experimentally achievable[36,51–53]. Based on the thirty independent non-adiabatic photo-reaction trajectories, we find that the light-driven diamond conversion of graphite is mainly achieved in the region close to the graphite damage threshold and requires sufficient and appropriate laser power. The longer the wavelength, the lower the required laser power (also see Suppl. Fig. 13). It can also be observed that within the fluence range where diamond structures are formed, the CD structure is more likely to be generated in the middle interval, while the HD structure is more prone to form in the upper and lower regimes. Laser fluence is directly related to the amount of electronic excitation and the specific modes of phonon excitation. Over-excitation leads to system collapse, while insufficient excitation fails to drive the graphite structure to overcome the reaction barrier and complete the phase transition. As indicated in the Suppl. Fig. 13, the electronic excitation level in the phase transitions that result in the formation of the CD or HD ranges from ~3.4% to 4.2%.

To gain further insight into the light-induced graphite-to-diamond phase transition mechanism revealed above, we compare the dynamic behavior of photoinduced structural transformation in graphite across different supercell sizes within the rt-TDDFT non-adiabatic computational framework, and the results show that the phase transition mechanism is essentially consistent (Suppl. Fig. 14). Compared to large

https://doi.org/10.1038/s41467-025-67064-1

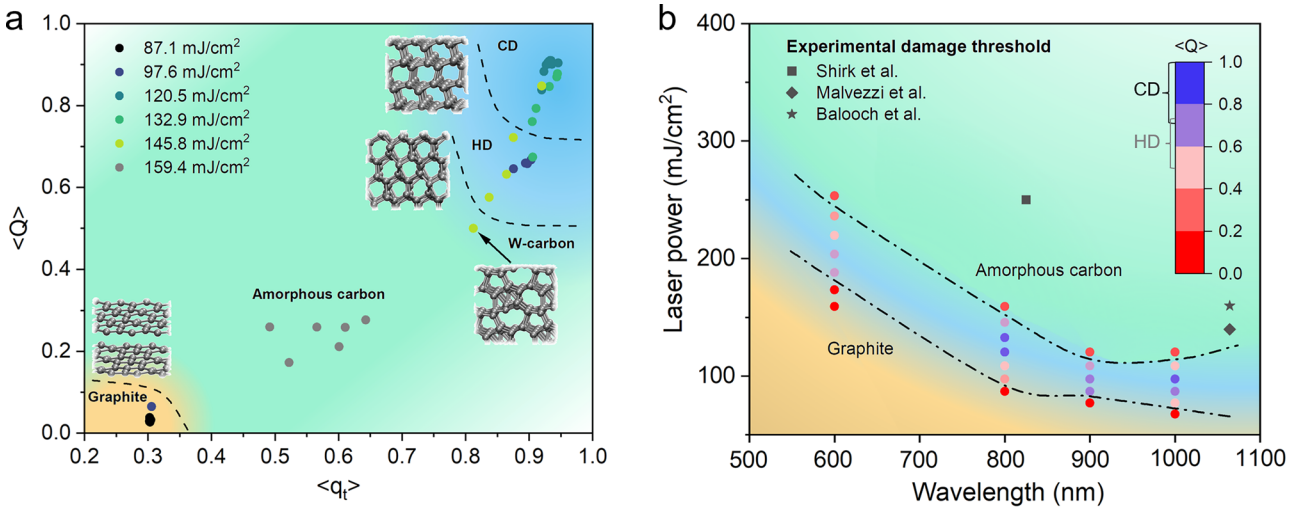

Fig. 5 | Phase diagram of light-driven graphite phase transition. a Fluence dependence of laser-induced graphite phase transition under a pump wavelength of 800 nm. Tetrahedral order parameter q_t and bond parameter Q are obtained by averaging from 300 to 400 fs in each trajectory. The dashed lines are guides for the eye to distinguish approximate boundaries of different carbon structures. **b** Optical modulation capability of the laser on the graphite phase transition. The bond parameter Q is used to distinguish CD and HD structures. $\langle Q \rangle$ ~1 stands for a perfect CD structure, and $\langle Q \rangle$ ~0.75 indicates a HD structure. Experimental values of graphite damage threshold are shown in black (refs. 36–38). The dash-dotted lines indicate the upper and lower boundaries of the laser fluence required to achieve a stable diamond structure at a given wavelength. Black and gray brackets indicate the approximate parameter ranges for forming CD and HD, respectively.

supercells or experimental scenarios, the direct interaction of laser pulses with the interior of small supercells is likely to trigger a faster and more sensitive response in phase transition simulations. Furthermore, investigations into the effects of laser polarization direction (Suppl. Fig. 15) and graphite defects indicate that laser irradiation with polarization perpendicular to the graphite plane barely generates sufficient excited electrons to induce phase transitions, while defects would also hinder the order-to-order phase transition process. These results imply that in the case of polycrystalline graphite, the existence of grain boundaries and high defect concentrations may substantially reduce the efficiency of the photoinduced graphite-to-diamond phase transition.

Discussion

Femtosecond Raman spectroscopy is expected to provide experimental verification for the mechanism of photoinduced graphite-to-diamond phase transition we proposed. This technique is developed to investigate ultrafast photoinduced structural changes in materials[54,55], and has been applied to reveal the nonequilibrium coupling between the E_{1u} and E_{2g} modes of the crystal lattice in bilayer and multilayer graphene[56], as well as the dynamics of short-lived transients in thin films[57].

Our first-principles non-adiabatic dynamic studies reveal the feasibility and dynamic pathways of light-induced graphite-to-diamond phase transition on ultrafast timescales and elucidate the microscopic mechanism of such nonequilibrium structural phase transition as well as the phase diagram for optical control. The direct electronic driving force for the light-induced diamond phase transition arises from the redistribution of excited charge carriers, and those scattered into high-energy orbitals result in the instability of the graphite structure. Meanwhile, the excitation of specific phonon modes induced by electron–phonon coupling plays a key role in the further evolution of the atomic structure, where the excitation of three induced phonon modes corresponding to the interlayer compression and sliding in the first stage is a prerequisite and necessary conditions for the transformation from sp^2 to sp^3 bonds. Subsequently, the further phonon–phonon coupling induces specific new phonon excitation, and the level of excitation determines the fine structure of the ultimate phase transition products, such as CD or HD structures. The proposed wavelength-fluence phase diagram for light-induced diamond formation demonstrates the capability and rule of ultrafast lasers with appropriate wavelength and power in optically modulating the phase transition. Our results provide a clear physical picture of how photo-excited charge carriers, through electron–phonon interactions, couple with induced lattice motions to drive the evolution of atomic structures. The proposed fundamental laws and reaction phase diagrams for light-induced diamond formation provide a priori basis for achieving precise optical synthesis.

Methods

First-principles excited-state molecular dynamics simulations

First-principles non-adiabatic molecular dynamics simulations were performed using time-dependent ab initio package (TDAP)[58,59], where the electron dynamics are captured within the framework of real-time time-dependent density functional theory (rt-TDDFT) and the coupled motion of electrons and nuclei is described by Ehrenfest dynamics[60]. Graphite crystal is simulated with a $2\times\sqrt{3}\times1$ supercell, containing two *AB* stacked sublayers of 16 carbon atoms. The initial lattice dimensions of the supercell are 4.92, 4.26, and 6.80 Å, respectively, and the graphite interlayer distance is 3.40 Å. Numerical atomic orbital basis set with double zeta polarization (DZP) and Troullier-Martins pseudopotentials are adopted. We employ the local density approximation (LDA)[61] to describe the electronic exchange-correlation energy. An auxiliary real-space grid equivalent to a plane-wave cutoff of 150 Ry is used, and the Brillouin zone is sampled by a $4\times4\times3$ $\boldsymbol{k}$-mesh. Linearly polarized laser pulse is applied along the armchair direction (*y*-axis) of graphite, with a Gaussian-enveloped waveform $E=E_0\cos(\omega t)\exp[-(t-t_0)^2/2\sigma^2]$, where the photon energy $\hbar\omega$ is 1.55 eV, field intensity $E_0=0.514$ V/Å at time $t_0=48$ fs. The timestep of 0.04 fs is applied for both electron and ion motions, evolving in a constant pressure-energy (NPE) ensemble, where pressure is controlled by the Parrinello-Rahman method[62]. After the light field irradiation, the total energy of the system remains essentially constant, with only a slight drifting of ~0.0002 eV/fs per atom caused by the accumulation of numerical errors.

Band structure and phonon calculations

Band structures are calculated via Vienna Ab Initio Simulation Package (VASP)[63] adopting the projector augmented wave (PAW) method. Phonon frequency and eigenvectors are calculated within density functional perturbation theory (DFPT) using PHONPY[64].

Born–Oppenheimer molecular simulation and structural relaxation

The structure relaxation from metastable light-induced product configuration is performed with CP2K package[65]. Initial atomic structure, velocities and temperature for the annealing simulation is obtained from the configuration of the non-adiabatic rt-TDDFT simulation at 400 fs. All configurations are annealed to room temperature by an 8 ps constant-pressure Born-Oppenheimer MD simulation with a cooling rate of 300 K/ps and a timestep of 0.1 fs, to achieve the state of stable carbons structure. Valence electron wave functions are expanded in a single zeta Gaussian basis set (SZV)[66]. Goedecker-Teter-Hutter (GTH) pseudopotentials[67] and BLYP exchange-correlation functional[68,69] are used.

Data availability

The source data of the main Figures in this paper are included as Source Data. Additional information can be obtained by contacting the corresponding author. Source data are provided with this paper.

References

1. Luo, K. et al. Coherent interfaces govern direct transformation from graphite to diamond. *Nature* **607**, 486–491 (2022).
2. Chen, G. W. et al. The transformation mechanism of graphite to hexagonal diamond under shock conditions. *JACS Au* **4**, 3413–3420 (2024).
3. Chen, D. et al. General approach for synthesizing hexagonal diamond by heating post-graphite phases. *Nat. Mater.* **24**, 513–518 (2025).
4. Scandolo, S., Bernasconi, M., Chiarotti, G. L., Focher, P. & Tosatti, E. Pressure-induced transformation path of graphite to diamond. *Phys. Rev. Lett.* **74**, 4015–4018 (1995).
5. Banhart, F. & Ajayan, P. M. Carbon onions as nanoscopic pressure cells for diamond formation. *Nature* **382**, 433–435 (1996).
6. Khaliullin, R. Z., Eshet, H., Kühne, T. D., Behler, J. & Parrinello, M. Nucleation mechanism for the direct graphite-to-diamond phase transition. *Nat. Mater.* **10**, 693–697 (2011).
7. Nüske, R. et al. Transforming graphite to nanoscale diamonds by a femtosecond laser pulse. *Appl. Phys. Lett.* **100**, 043102 (2012).
8. Rossini, F. D. & Jessup, R. S. Heat and free energy of formation of carbon dioxide, and of the transition between graphite and diamond. *J. Res. Natl Bur. Stand.* **21**, 491–513 (1938).
9. Bundy, F. P., Hall, H. T., Strong, H. M. & Wentorf, R. H. Man-made diamonds. *Nature* **176**, 51–55 (1955).
10. Bundy, F. P. Direct conversion of graphite to diamond in static pressure apparatus. *Science* **137**, 1057–1058 (1962).
11. Bundy, F. P. Direct conversion of graphite to diamond in static pressure apparatus. *J. Chem. Phys.* **38**, 631–643 (1963).
12. Yagi, T., Utsumi, W., Yamakata, M.-A., Kikegawa, T. & Shimomura, O. High-pressure in situ x-ray-diffraction study of the phase transformation from graphite to hexagonal diamond at room temperature. *Phys. Rev. B* **46**, 6031–6039 (1992).
13. Bundy, F. P. & Kasper, J. S. Hexagonal diamond—a new form of carbon. *J. Chem. Phys.* **46**, 3437–3446 (1967).
14. DeCarli, P. S. & Jamieson, J. C. Formation of diamond by explosive shock. *Science* **133**, 1821–1822 (1961).
15. Gust, W. H. Phase transition and shock-compression parameters to 120 GPa for three types of graphite and for amorphous carbon. *Phys. Rev. B* **22**, 4744–4756 (1980).
16. Morris, D. G. An investigation of the shock-induced transformation of graphite to diamond. *J. Appl. Phys.* **51**, 2059–2065 (1980).
17. Hirai, H., Kukino, S. & Kondo, K.-I. Predominant parameters in the shock-induced transition from graphite to diamond. *J. Appl. Phys.* **78**, 3052–3059 (1995).
18. Erskine, D. J. & Nellis, W. J. Shock-induced martensitic phase transformation of oriented graphite to diamond. *Nature* **349**, 317–319 (1991).
19. Armstrong, M. R. et al. Highly ordered graphite (HOPG) to hexagonal diamond (lonsdaleite) phase transition observed on picosecond time scales using ultrafast x-ray diffraction. *J. Appl. Phys.* **132**, 055901 (2022).
20. Yang, L. et al. Synthesis of bulk hexagonal diamond. *Nature* **644**, 370–375 (2025).
21. Han, Q., Luo, K., Gao, Q., Wu, Y. & He, J. Theoretical study on phase transition of various graphitic structures under high pressure. *Diam. Relat. Mater.* **133**, 109725 (2023).
22. Wang, J. et al. Graphite/diamond transformation mechanism under the action of an iron-based catalyst. *CrystEngComm* **25**, 1884–1893 (2023).
23. Li, B. et al. Discovery of gradia between graphite and diamond. *Acc. Mater. Res.* **5**, 614–624 (2024).
24. Sun, H. et al. Understanding the mechanism of shockwave induced graphite-to-diamond phase transition. *Materialia* **24**, 101487 (2022).
25. Volz, T. J. & Gupta, Y. M. Elastic moduli of hexagonal diamond and cubic diamond formed under shock compression. *Phys. Rev. B* **103**, L100101 (2021).
26. Nakayama, H. & Katayama-Yoshida, H. Ab initio design on the diamond synthesis method by core excitation. *Jpn. J. Appl. Phys.* **41**, L817–L819 (2002).
27. Nakayama, H. & Katayama-Yoshida, H. Direct conversion of graphite into diamond through electronic excited states. *J. Phys. Condens. Matter* **15**, R1077–R1091 (2003).
28. Raman, R. K. et al. Direct observation of optically induced transient structures in graphite using ultrafast electron crystallography. *Phys. Rev. Lett.* **101**, 077401 (2008).
29. Carbone, F., Kwon, O.-H. & Zewail, A. H. Dynamics of chemical bonding mapped by energy-resolved 4D electron microscopy. *Science* **325**, 181–184 (2009).
30. Luo, D. et al. Ultrafast formation of a transient two-dimensional diamondlike structure in twisted bilayer graphene. *Phys. Rev. B* **102**, 155431 (2020).
31. Kanasaki, J., Inami, E., Tanimura, K., Ohnishi, H. & Nasu, K. Formation of sp^3-bonded carbon nanostructures by femtosecond laser excitation of graphite. *Phys. Rev. Lett.* **102**, 087402 (2009).
32. Inami, E., Nishioka, K. & Kanasaki, J. Atomic-scale view of the photoinduced structural transition to form sp^3-like bonded order phase in graphite. *Sci. Rep.* **13**, 21439 (2023).
33. Nasu, K. sp^3 domain in graphite by visible light and photoinduced phase transitions. *Eur. Phys. J. B* **75**, 415–430 (2010).
34. Dong, X. et al. An ab initio study on the transition paths from graphite to diamond under pressure. *J. Phys. Condens. Matter* **25**, 145402 (2013).
35. Song, C. et al. Driving forces for ultrafast laser-induced sp^2 to sp^3 structural transformation in graphite. *Npj Comput. Mater.* **9**, 76 (2023).
36. Shirk, M. D. & Molian, P. A. Ultra-short pulsed laser ablation of highly oriented pyrolytic graphite. *Carbon* **39**, 1183–1193 (2001).
37. Malvezzi, A. M., Bloembergen, N. & Huang, C. Y. Time-resolved picosecond optical measurements of laser-excited graphite. *Phys. Rev. Lett.* **57**, 146–149 (1986).
38. Balooch, M., Schildbach, M., Tench, R., Allen, M. & Siekhaus, W. J. Surface site specificity on the basal plane of graphite: 1.06 μm laser damage threshold and reactivity with oxygen between 350 and 2300. *K. J. Vac. Sci. Technol. B* **9**, 1088–1091 (1991).

39. Mankowsky, R. et al. Nonlinear lattice dynamics as a basis for enhanced superconductivity in $YBa_2Cu_3O_{6.5}$. *Nature* **516**, 71–73 (2014).
40. Gedik, N., Yang, D. S., Logvenov, G., Bozovic, I. & Zewail, A. H. Nonequilibrium phase transitions in cuprates observed by ultrafast electron crystallography. *Science* **316**, 425–429 (2007).
41. Errington, J. R. & Debenedetti, P. G. Relationship between structural order and the anomalies of liquid water. *Nature* **409**, 318–321 (2001).
42. Zhou, G., Lu, G. & Prezhdo, O. V. Modeling Auger processes with nonadiabatic molecular dynamics. *Nano Lett.* **21**, 756–761 (2020).
43. Mishina, T., Nitta, K. & Masumoto, Y. Coherent lattice vibration of interlayer shearing mode of graphite. *Phys. Rev. B* **62**, 2908–2911 (2000).
44. Shin, D. Recent studies on the light-induced phenomena in condensed matter systems and related numerical tools. *J. Korean Phys. Soc.* **81**, 707–714 (2022).
45. Shin, D. et al. Dynamical amplification of electric polarization through nonlinear phononics in 2D SnTe. *Npj Comput. Mater.* **6**, 182 (2020).
46. Gu, M. & Rondinelli, J. M. Nonlinear phononic control and emergent magnetism in Mott insulating titanates. *Phys. Rev. B* **98**, 024102 (2018).
47. Shuai, W.-J., Wang, R. & Zhao, J.-Z. Ferroelectric phase transition driven by anharmonic lattice mode coupling in two-dimensional monolayer In_2Se_3. *Phys. Rev. B* **107**, 155427 (2023).
48. Li, Q. et al. Superhard monoclinic polymorph of carbon. *Phys. Rev. Lett.* **102**, 175506 (2009).
49. Boulfelfel, S. E., Zhu, Q. & Oganov, A. R. Novel sp^3 forms of carbon predicted by evolutionary metadynamics and analysis of their synthesizability using transition path sampling. *J. Superhard Mater.* **34**, 350–359 (2013).
50. Niu, H. et al. Families of superhard crystalline carbon allotropes induced via cold-compressed graphite and nanotubes. *Phys. Rev. Lett.* **108**, 135501 (2012).
51. Kirkwood, S. E., van Popta, A. C., Tsui, Y. Y. & Fedosejevs, R. Single and multiple shot near-infrared femtosecond laser pulse ablation thresholds of copper. *Appl. Phys. A* **81**, 729–735 (2005).
52. Kemp, A. J. & Divol, L. Interaction physics of multipicosecond Petawatt laser pulses with overdense plasma. *Phys. Rev. Lett.* **109**, 195005 (2012).
53. Li, Z., Leng, Y. & Li, R. Further development of the short-pulse petawatt laser: trends, technologies, and bottlenecks. *Laser Photon. Rev.* **17**, 2100705 (2022).
54. Yoshizawa, M. & Kurosawa, M. Femtosecond time-resolved Raman spectroscopy using stimulated Raman scattering. *Phys. Rev. A* **61**, 013808 (1999).
55. Kuramochi, H. & Tahara, T. Tracking ultrafast structural dynamics by time-domain Raman spectroscopy. *J. Am. Chem. Soc.* **143**, 9699–9717 (2021).
56. Buchenau, S. et al. Optically induced avoided crossing in graphene. *Phys. Rev. B* **108**, 075419 (2023).
57. Takaya, T., Enokida, I., Furukawa, Y. & Iwata, K. Near-infrared resonance stimulated Raman study of short-lived transients in PTB7 films. *Vib. Spectrosc.* **106**, 103011 (2020).
58. Lian, C., Guan, M., Hu, S., Zhang, J. & Meng, S. Photoexcitation in solids: first-principles quantum simulations by real-time TDDFT. *Adv. Theory Simul.* **1**, 1800055 (2018).
59. You, P., Chen, D., Lian, C., Zhang, C. & Meng, S. First-principles dynamics of photoexcited molecules and materials towards a quantum description. *WIREs Comput. Mol. Sci.* **11**, e1492 (2021).
60. Curchod, B. F., Rothlisberger, U. & Tavernelli, I. Trajectory-based nonadiabatic dynamics with time-dependent density functional theory. *ChemPhysChem* **14**, 1314–1340 (2013).
61. Ceperley, D. M. & Alder, B. J. Ground state of the electron gas by a stochastic method. *Phys. Rev. Lett.* **45**, 566–569 (1980).
62. Parrinello, M. & Rahman, A. Polymorphic transitions in single crystals: a new molecular dynamics method. *J. Appl. Phys.* **52**, 7182–7190 (1981).
63. Kresse, G. & Furthmüller, J. Efficient iterative schemes for ab initio total-energy calculations using a plane-wave basis set. *Phys. Rev. B* **54**, 11169 (1996).
64. Togo, A. & Tanaka, I. First principles phonon calculations in materials science. *Scr. Mater.* **108**, 1–5 (2015).
65. Kuhne, T. D. et al. CP2K: An electronic structure and molecular dynamics software package - Quickstep: efficient and accurate electronic structure calculations. *J. Chem. Phys.* **152**, 194103 (2020).
66. VandeVondele, J. & Hutter, J. Gaussian basis sets for accurate calculations on molecular systems in gas and condensed phases. *J. Chem. Phys.* **127**, 114105 (2007).
67. Goedecker, S., Teter, M. & Hutter, J. Separable dual-space Gaussian pseudopotentials. *Phys. Rev. B* **54**, 1703–1710 (1996).
68. Becke, A. D. Density-functional exchange-energy approximation with correct asymptotic behavior. *Phys. Rev. A* **38**, 3098–3100 (1988).
69. Lee, C., Yang, W. & Parr, R. G. Development of the Colle-Salvetti correlation-energy formula into a functional of the electron density. *Phys. Rev. B Condens. Matter* **37**, 785–789 (1988).

Acknowledgements

This work is supported by the National Key R&D Program of China under Grant Nos. 2021YFA1400503 (C.Z.) and 2021YFA1400201 (S.M. and C.Z.), National Natural Science Foundation of China under Grant Nos. 12025407 (S.M.), 12574278(C.Z.), and CAS Project for Young Scientists in Basic Research YSBR-047 (C.Z. and S.M.).

Author contributions

Y.J., C.Z., and S.M. proposed the project. C.Z. and S.M. conceived and supervised this project. Y.J. carried out the simulations and performed the analysis. Y.J., C.S., D.C. and Q.C. developed methodologies and analysis codes. Y.J., C.Z., and S.M. interpreted the analysis and wrote the manuscript. All authors contributed to the discussions and revisions of the manuscript.

Competing interests

The authors declare no competing interests.

Additional information

Supplementary information The online version contains supplementary material available at https://doi.org/10.1038/s41467-025-67064-1.

Correspondence and requests for materials should be addressed to Cui Zhang or Sheng Meng.

Peer review information *Nature Communications* thanks Artem Oganov, Jianguo Wen, and the other, anonymous, reviewer(s) for their contribution to the peer review of this work. A peer review file is available.